UNIVERSITY *of* York

This is a repository copy of *Characterization of Electrical-Thermal-Mechanical Deformation of Bonding Wires under Silicone Gel Using LF-OCT*.

White Rose Research Online URL for this paper:
https://eprints.whiterose.ac.uk/189137/

Version: Accepted Version

Article:

White Rose
university consortium
Universities of Leeds, Sheffield & York

eprints@whiterose.ac.uk
https://eprints.whiterose.ac.uk/

Characterisation of Electrical-Thermal-Mechanical Deformation of Bonding Wires Under Silicone Gel Using LF-OCT

Zhiyi Zhao, Zijian Zhang, Samuel Lawman, Zhihao Yin, Yihua Hu, *Senior Member, IEEE*, Ju Xu, and Yaochun Shen

Abstract-Bonding wires are one of the most failure-prone components of power electronics modules (PEMs), and silicone gel is usually employed to encase bonding wires. To study the deformation of silicone gel-encased bonding wires, in this paper we report the use of line-field optical coherence tomography (LF-OCT) technique to precisely measure the electrical-thermal-mechanical (ETM) deformation of bonding wires. A LF-OCT system was developed to capture the whole cross-sectional image (B-scan) of the bonding wire sample in a single shot fashion due to its advantageous parallel detection scheme. This, together with the Fourier phase self-referencing technique, allows the deformation of the bonding wires to be quantitatively measured down to the range of 0.1 nm. The maximum sampling rate (framerate) of the deformation measurement achieved was 400 Hz when setting camera imaging size to 1920×200 pixels, providing a temporal resolution of 2.5 ms for monitoring the ETM deformation dynamics of the bonding wire. We found that the ETM deformation of the gel-encased bonding wire was about three times smaller than that of the bare bonding wire. These results represent the first experimental demonstration that the LF-OCT could be a useful analytical tool for studying the time-dependent ETM deformation of bonding wires encased by silicone gel.

Index Terms-Bond wire reliability, silicone gel, electrical-thermal-mechanical deformation, line-field optical coherence tomography (LF-OCT)

I. INTRODUCTION

Power electronics modules (PEMs) are widely employed as switching semiconductor devices in renewable energy generation and transport electrification [1]. Since PEMs are usually applied in safety and mission-critical scenarios such as electric trains, aerospace, and offshore wind power, the reliability of PEM is of significant interest to academia and industry [2-4]. The wire-bonding technique is the most widely used method for the packaging of PEMs [2, 5], which employs bonding wires to provide the electrical connections between the output terminals and semiconductor dies. In addition, silicone gel is usually used in PEMs to provide dielectric insulation [6]. Nevertheless, bonding wires are still one of the most fragile components in wire-bonding packaged PEMs [5, 7]. The reliability problems of bonding wires are mainly caused by electrical-thermal-mechanical (ETM) stress during power cycling [2, 8, 9]. The operation current cycles in PEMs induce the repetitive heating, which causes the repetitive ETM deformation of bonding wires leading to fatigue issues in them. The failures of bonding wires reduce the PEM lifetime, which in turn affects the reliability of the whole system served by the PEM. Therefore, there has been considerable interest in studying the effect of ETM stress on the reliability of bonding wires and PEMs [10-12].

Several experimental techniques have been reported to investigate the effect of repetitive ETM deformation of bonding wires, such as scanning electron microscope (SEM), X-ray computed tomography (X-ray CT), infrared (IR) thermography, and laser Doppler vibrometer (LDV). SEM is usually applied to observe the failures and microstructural changes of components under different cycles of the power cycling test [13, 14]. For instance, SEM images can reveal the cracks initiated in wire-die joint. This would involve cutting the sample and taking SEM images. Thus, this method is destructive in nature. X-ray CT acquires tomographic images of the wire-die joint to also measure cracking induced by different power cycles, but in a non-destructive way [15]. However, both SEM and X-ray CT techniques are only suitable for static measurements, and they cannot be used for measuring directly the dynamic changes of the bonding wires when electrical current pulses are applied to a PEM. IR thermography can measure the temperature fluctuations of bonding wires and thermal distribution in a PEM [16, 17], and the bonding wire failures can be detected by analysing thermal characteristics. However, IR thermography only measures the surface temperature and it does not provide any direct measurement of the resultant ETM deformation. LDV, on the other hand, can be used to measure the vertical displacement of a surface point on the bonding wire under different operation conditions [18], facilitating the reliability investigation of bonding wires. Both IR thermography and LDV are thus suitable for dynamic measurements of PEM, albeit IR cameras usually measure the surface temperature distribution, and LDV measures the surface vibration of PEM without silicone gel.

In addition to these experimental measurement methods, theoretical simulation methods, such as finite element modelling (FEM), have also been applied to investigate the influence of

Z.Y. Zhao, Z.J. Zhang, S. Lawman, and Y.C. Shen are with the Department of Electrical Engineering and Electronics, University of Liverpool, Liverpool L69 3GJ, UK (e-mail: sgzzha35@liverpool.ac.uk; Z.Zhang116@liverpool.ac.uk; S.Lawman@liverpool.ac.uk; Y.C.Shen@liverpool.ac.uk)

Y.H. Hu is with Department of Electronic Engineering, University of York, York YO10 5DD, UK (e-mail: yihua.hu@york.ac.uk)

Z.H. Yin, J. Xu are with Beijing Engineering Laboratory of Electrical Drive System & Power Electronic Device Packaging Technology, Micro-Nano Fabrication Technology Department, Institute of Electronic Engineering, Chinese Academy of Sciences, Beijing 100190, China, and University of Chinese Academy of Sciences, Beijing, China (e-mail: yinzhihao20@mails.ucas.ac.cn; xuju@mail.iee.ac.cn)

ETM stress on bonding wire reliability by simulating the thermal/stress distribution and mechanical deformation of wires [19-21]. Moreover, FEM is utilised as the cross-validation method for IR thermography and LDV measurements, although the experimental results are limited to samples without silicone gel. Since the thermal conductivity and mechanic properties of encapsulant affect the reliability and lifetime of PEMs [22, 23], the influence of silicone gel should be considered. Several studies based on FEM have been carried out to investigate the reliability of bonding wires encased by silicone gel [6] and globtop [24]. Nevertheless, there is a need of more experimental validation of the simulated ETM deformation of silicone gel-encased bonding wires.

Optical coherence tomography (OCT) [25] systems have previously been studied as a tool for the non-destructive inspection of electronics products. Scanning-point OCT systems have been applied to inspect the shape of antennas and detect voids in encapsulant [26, 27]. Swept-source OCT was applied to measure the coefficient of thermal expansion (CTE) of polystyrene resin in light-emitting diode packaging [28]. Yaqoob et al. [29] proposed a spectral-domain line-field phase microscope to measure the motion of biological cell membranes. The phase of multiple lateral points on the line-illumination was measured simultaneously and the self-referencing method was proposed to suppress the phase noise. The spectral-domain line-field (LF-) OCT [30] system is advantageous in the investigation of bonding wire deformation under silicone gel. LF-OCT, because of its line-field illumination and 2D imaging spectrograph parallel detection, can acquire the whole cross-sectional image of the bonding wire in a single shot fashion without the need of mechanical scanning. The displacement/deformation of the bonding wire can be measured with sub-nanometre sensitivity by extracting phase information recorded in the raw OCT spectra.

In this paper, we report the first experimental demonstration that the nano-scale deformation of bonding wires under silicone gel can be directly measured by a LF-OCT system. The global shuttered LF-OCT system and phase self-referencing method employed in this study provides real-time B-scan tomography with sub-nanometre displacement phase stability. It was found that LF-OCT can measure not only the surface displacement of the bare bonding wire, but also the deformation of gel-encased bonding wires, with a measurement sensitivity of 0.1 nm and a temporal resolution of 2.5 ms. This provides a unique analytical method for studying ETM deformation of gel-encased bonding wires.

II. METHODS AND EXPERIMENT

A. System and Experiment Setup

Fig. 1(a) shows a schematic diagram of the LF-OCT system and pulse generation circuit module used in the study. The optical configuration of LF-OCT is similar to our previous work [31, 32], but a low-cost infrared superluminescent diode (SLED) of 50 nm spectral bandwidth centred at 840 nm was used. Line-field illumination is achieved by a cylindrical lens. A 50:50 beam splitter was used to split the light into the sample and reference arms, where two identical achromatic doublet lenses

were used to minimise the dispersion mismatch between the two arms. The reflected light from the sample and reference arms was recombined and directed to an imaging spectrograph that comprised of a 10-μm wide entrance slit, a transmission grating with 1200 lines/mm, two lenses and a CMOS camera. The LF-OCT configuration facilitates parallel detection of depth profiles (A-scans) with a single exposure [30], which can significantly reduce the motion-induced image distortion and artefacts. In addition, a data acquisition card (National Instruments, NI USB-6009) was used to synchronise the data acquisition and the driving electrical current pulses that were produced by using a constant current source (Thurlby Thandar Instruments, EX354RD). A custom MATLAB program was developed to operate the LF-OCT system. Fig. 1(b) shows a photograph of the LF-OCT system used.

The axial resolution of the LF-OCT, defined as the full width at half maximum (FWHM) of the axial point spread function after performing a Gaussian fit (see Fig. 1(c)), was determined to be 8 μm. The lateral resolution of the LF-OCT was determined to be 17.5 μm (line pair width) by measuring a USAF 1951 resolution target, where the element 6 in the group 5 was resolved (indicated by red box in Fig. 1(d)). The phase stability of the LF-OCT was determined to be 0.0012 rad, corresponding to a minimum detectable deformation of 0.1 nm. The upper limit of the measurable displacement is over 2 mm, which is ultimately limited by the imaging depth of the developed LF-OCT system.

The length of the line illumination is 7 mm on the sample by setting the camera ROI to its full 1920×1200 pixels, which is enough to cover heavy bonding wire and die surface in PEMs. In this study, the region of interest (ROI) of the camera was set to 1920×200 pixel corresponding to a line length of 1.2 mm, which is sufficient to cover the region of the wire and part of the glass substrate. The maximum framerate under this camera ROI setting was 400 Hz, providing a temporal sampling resolution of 2.5 ms. According to Nyquist sampling law, vibrational signal with a frequency up to 200 Hz can be resolved with the framerate of 400 Hz. This framerate is currently limited by the data transfer rate between the camera used and the computer. The exposure time for each B-scan is 0.25 ms, corresponding to a maximum possible framerate of 4000 fps for the current optical design. We note that a LF-OCT with a high-speed camera, a framerate of 2500 fps has been reported [33], thus with the addition of a high-speed camera the proposed LF-OCT technique has the potential to characterise ETM deformation of bonding wires with a frequency of over 1000 Hz.

B. Sample and Experiment Design

In order to demonstrate the deformation measurement performance of the LF-OCT system, a custom simplified bonding wire sample was used. Specifically, a single copper wire was fixed on a glass substrate (Fig. 2(a)). The wire had a 120 μm diameter, and the highest point of the wire loop was 1.1 mm above the glass substrate. The use of a single wire minimised the influence of uneven current distribution thus helped accurate quantification of the electrical current value flowing through the wire. As a result, the wire ETM deformation under
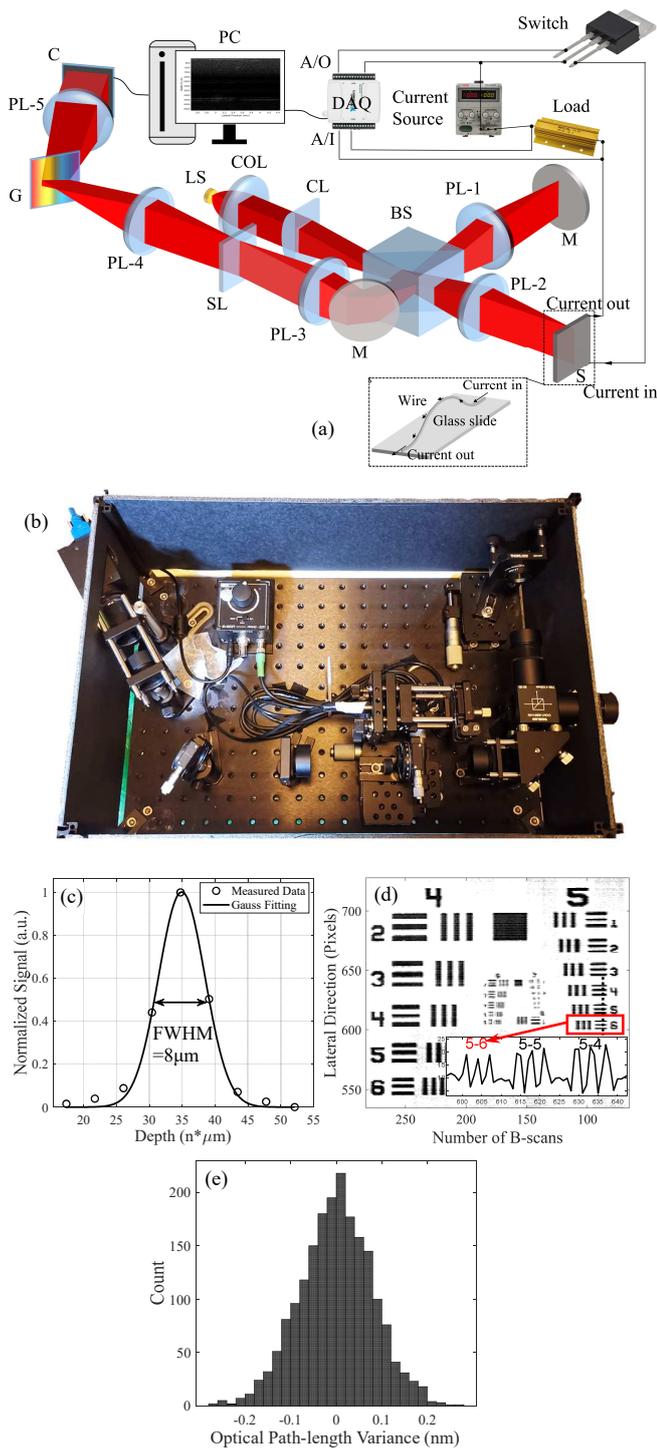
Fig. 1. (a) LF-OCT system and pulse-current generation setup. LS – Light source; Col – Collimator; CL – Cylindrical lens; BS – 50:50 Beam splitter; PL – Plano-convex Lens 1&2: objective lens 3: collection lens 4&5 Spectrograph lens; M –Silver Mirror; S – Sample; SL – Slit; G – Grating; C – Camera; PC – System control; DAQ – Data Acquisition Card. (b) Photograph of the inhouse-built LF-OCT; (c) Axial resolution; (d) Lateral resolution - the red box indicates that the Group 5 Number 6 element of a USAF 1951 resolution target can be clearly distinguished, indicating a lateral resolution of 17.5 µm; (e) Phase stability of the system.
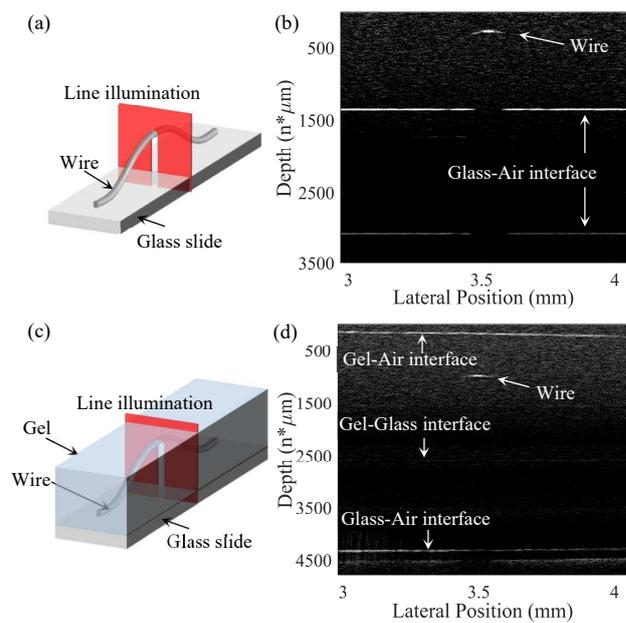
Fig. 2. The schematic diagram (a) and OCT B-scan image (b) of bare bonding wire sample; The schematic diagram (c) and OCT B-scan image (d) of silicone gel-encased bonding wire sample.

the specific pulse current measured by LF-OCT system could be used to compare with the simulated results. The loop geometry of wire in the sample simulated the bonding wire in PEM, and two terminals of the wire were fixed on a glass slide substrate by instant glue. The low CTE and electrical insulation of glass substrate suggests that the measurement deformation was dominated by the ETM deformation of the bonding wire. Moreover, the single wire configuration prevented Lorentz force from affecting the wire deformation. Fig. 2 shows the measurement schematic diagram and the typical B-scan images of bare wire and gel-encased wire.

The wire with a diameter of 120 µm was used in all experiments to eliminate influence from the different wire geometry profile. The deformation of the wire was measured at the vertex around the central position on the wire loop because the top of the wire loop has the maximal vertical displacement [18] and maximal temperature [34]. Since the amplitudes, duty cycles, and frequencies of the electrical current pulses flowing in the bonding wire are different during practical applications and power cycling tests, the ETM deformations induced by different pulse current were measured. After acquiring the deformation data of the bare wire under different pulse current, the silicone gel (Evostik) was added to encase the wire. Afterwards, the deformations of the gel-encased wire under the same set of pulse current parameters were measured.

The sample was fixed during the experiment to eliminate the axial position or any mechanical movement errors. The system was placed on an optical table to reduce random vibration errors. The room temperature during the experiments was around 19 °C.

Refractive index of the applied silicone gel was measured according to the published method [35]. In brief, the gel was

dropped on a glass slide, and the B-scans were taken. The refractive index of the gel was calculated by dividing the real thickness (distance between the gel surface and glass surface) from the measured optical path length difference. The refractive index of the applied silicone gel was determined to be 1.39, which was close to the published value of the acetoxy silicone sealant [36]. In this study, the used refractive index values of air and the silicone gel are 1 and 1.39 respectively.

C. Data Processing

The procedure of data processing is shown in Fig. 3. The B-scan images (Fig. 3(b)) were reconstructed from the raw spectra (Fig. 3(a)) data set (I. in Fig. 3). Next, the peak value positions of each A-Scan corresponding to the top surface of the wire and the glass substrate (interface profile) were detected. The Fourier phase (complex phase angle of the pixel immediately after the Fourier transform) of a selected glass surface point, located away from the wire, was taken as the reference phase. This minimises possible phase changes of the reference point caused by the wire temperature fluctuations. The reference phase was then subtracted from the Fourier phase of the other pixels on the interface profile. As a result, the common-mode phase noise is removed by this self-referencing [29]. After extracting and unwrapping the phase in all B-scans, the time-dependent phase map (Fig. 3(c)) was acquired (II. in Fig. 3). The phase-microscopy theory [37, 38] or Fourier phase [39, 40] was applied to calculate the nano-scale displacement. Fig. 3(d) and (e) show the time-dependent phase and corresponding vertical displacement of a glass substrate point and a wire surface point, respectively. Since the glass substrate was not affected by the temperature fluctuation of the wire, the phase changes and corresponding vertical displacement were around zero (Fig. 3(d)). The ETM stress-induced vertical displacement of the wire is illustrated in Fig. 3(e).

For the spectral-domain OCT, assuming that the reflectivity of reference reflector (R_r) is much larger than the reflectivity of sample reflector (R_s), the interferogram detected by the camera can be expressed approximately as:

$$I(k) \propto (\rho/2)S(k)\sum_{i=1}^{N}\sqrt{R_r R_s(i)}\cos(2kn(z_i + \Delta z_i)) \quad (1)$$

Where k is the wavenumber, $S(k)$ encodes the power spectral dependence of the light source, ρ is the responsivity of the camera detector; N indicates the numbers of the sample reflectors; $R_s(i)$ is the power reflectivity of the i-th reflector in the sample; n is the group refractive index of the sample. ($z_i + \Delta z_i$) is the distance between reference reflector and i-th reflectors in the sample. Since the interferogram is discrete sampling by the detector, z_i is the visualised peak position or depth shown in A-scan and Δz_i is the deviation from i-th sample reflector. The result of a complex depth profile $i(z)$ is obtained by applying the discrete Fourier transform of the acquired interferogram. After removing the negative mirror terms, complex depth profile can be given as [37]:

$$i(z) \propto (\rho/4)S\sum_{i=1}^{N}\sqrt{R_r R_s(i)}E(2nz_i)\exp(j2nk_0\Delta z_i) \quad (2)$$
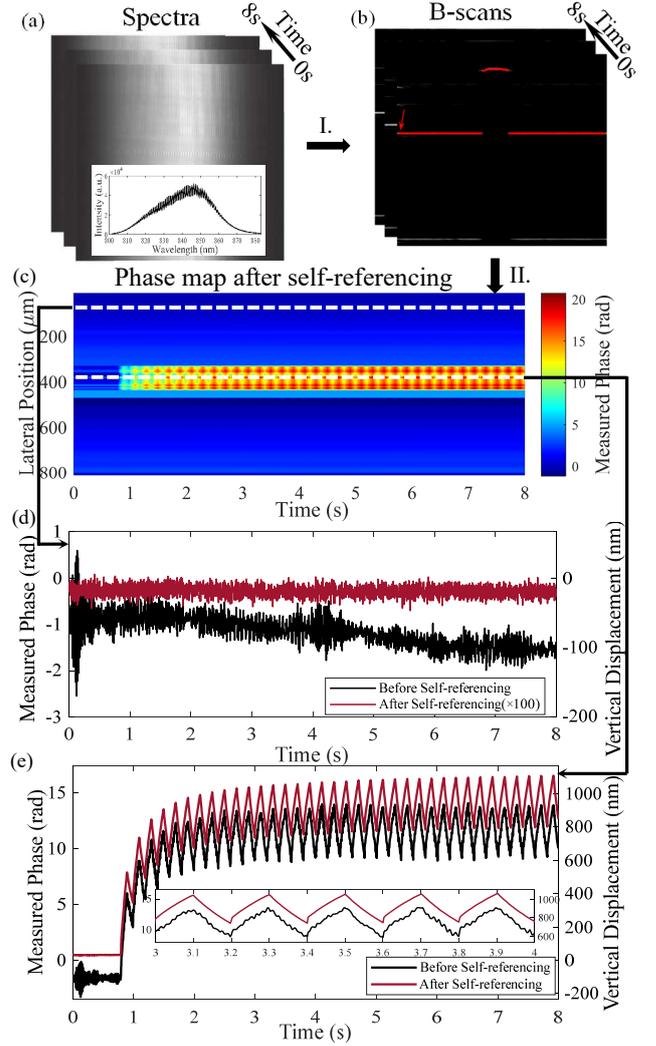
Fig. 3. Flow chart of data processing. I. B-scans reconstruction. II. Extract and unwrap phase. Apply phase self-referencing. (a) Acquired spectra from the spectrograph; (b) B-scans reconstructed from the acquired spectra. The peak positions were marked as red dots, and the selected reference point was indicated as a red arrow; (c) Time-dependent phase map of wire and glass surface points. Time-dependent phase and corresponding displacement of a point on (d) glass and (e) wire; The normal scale of glass displacement appears as a straight line. For better view, the result of glass displacement (after self-referencing) was multiplied by 100. Black line - Phase/displacement without self-referencing; Red line - Phase/displacement after self-referencing.

S is the total source power; E is the coherence envelop function. k_0 is the centre wavenumber of the light source. Thus, the deviation Δz_i for the reflector at depth z_i can be extracted from the phase of $i(z)$ [37]:

$$\Delta z_i = \frac{\varphi(z_i)}{2nk_0} \quad (3)$$

$\varphi(z_i)$ denotes the phase angle of $i(z_i)$. Finally, the measured phase would be converted to the displacement by applying (3)

III. RESULTS AND DISCUSSION

A. Time-resolved Wire Deformation

Fig. 4 shows the measured deformation characteristics of both bare wire and gel-encased wire, under power cycling of 1s and continued 5 Hz current pulses, respectively. The measured pulse current sequence is also displayed in Fig. 4. It can be seen that during each current pulse, the vertical displacement of the wire increases due to ETM deformation, e.g., the wire expands because of electrical heating. The vertical displacement of the wire decreases when there is no current pulse. However, the vertical displacement of the wire does not go to zero during the 0.1 s cooling period.

To help the analysis of the deformation characteristics, we define the following three parameters: (1) the max displacement (MD) is defined as the maximum value in the vertical displacement curve, (2) the periodic displacement is defined as the displacement induced by each electrical current pulse, (3) the vibration amplitude (VA) is defined as the peak-to-peak amplitude of a periodic displacement (see Fig. 4(b)). The MD represents to the maximum strain on the wire whilst the VA represents to the repetitive strain on the wire. Fig. 4 indicates that the wire under silicone gel has a lower VA and MD. Furthermore, the heating/cooling process is also different between the bare wire and gel-encased wire. This can be explained by the fact that the gel has a larger thermal conductivity than the air, thus the heat generated in the wire will be dissipated faster into the gel and absorbed there. In addition, unlike the bare wire, which is free to move, the movement of the gel-encased wire will be limited by the silicone gel.
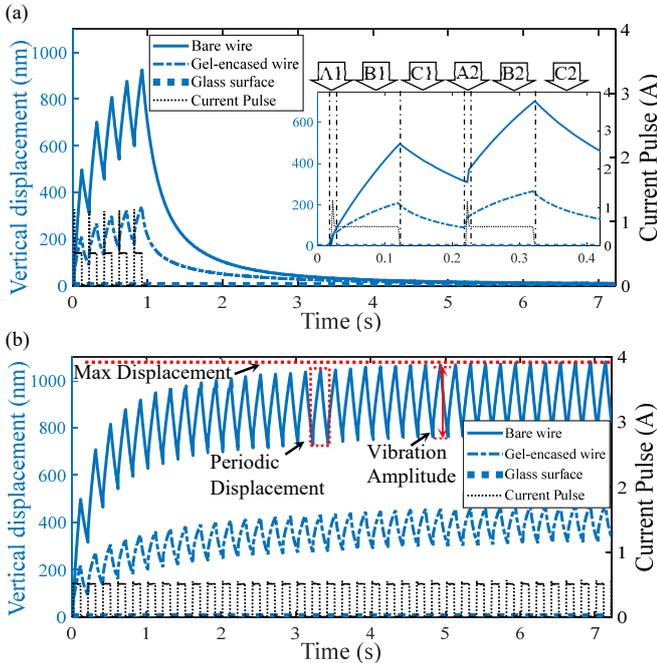
The zoomed image in Fig. 4(a) shows the first two periodic displacement profiles caused by electrical current pulse. The periodic displacement can be divided into three stages (A, B, C). Stage A represents the displacement produced by the transient peak current in the circuit. Stage B stands for the displacement induced by the high-level current of each pulse. The displacement in stage C is the result of no current cooling process. The total vertical displacement is produced by the accumulation of stage A-B-C. Although the transient peak current exists at the beginning of each pulse, the dominant factor for the displacement is the high-level current of each pulse. Additionally, the displacement on the glass surface is shown as a flat line in Fig. 4, which indicates that the glass surface is static and not affected by the thermal dissipation from the wire.

B. Wire Deformation Characteristics under Different Current Amplitudes, Frequencies, and Duty Cycles

In order to analyse the influence of different current amplitudes, frequencies, and duty cycles on the deformation of wire under-tested, various current loads were added to the wire. The wire deformation characteristics with various pulse current amplitudes are shown in Fig. 5. The values of the MD and the VA increase with the increase of pulse current amplitude. This is as expected because larger current generates more heats in the wire. In addition, since 100 mA is much smaller than the amplitude of transient peak current in the employed circuit, the transient peak current dominates the deformation of the wire. Thus, the shape of the 100 mA displacement curve is different

Fig. 4. (a) Displacement of the wire under 1 s, 5 Hz, 500 mA Pulse current (blue- bare wire, dotted blue – gel-encased wire, bold dash blue – reference point) (b) Displacement of the wire under 5 Hz, 500 mA Pulse current (blue-bare wire, dotted blue – gel-encased wire, bold dash blue – reference point).
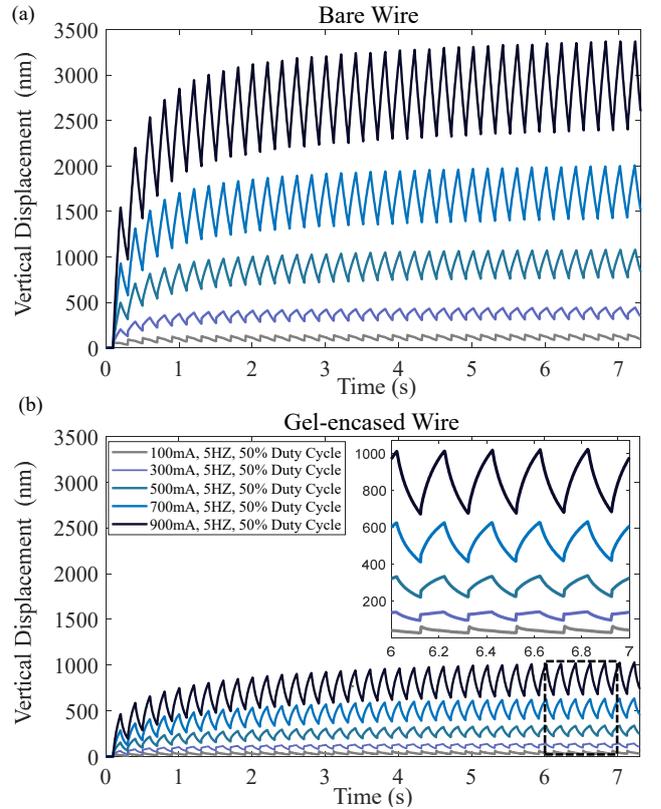
Fig. 5. Vertical displacement of wire under different pulse current amplitudes, (a) bare wire; (b) encased with silicone gel.

(a)

MD (Bare wire) =3751.9581*x^2+302.7812*x

MD (Gel-encased wire) =1082.9575*x^2+158.8913*x

(b)

MVA (Bare wire) =1091.9415*x^2+83.9282*x

MVA (Gel-encased) =360.1295*x^2+55.7327*x
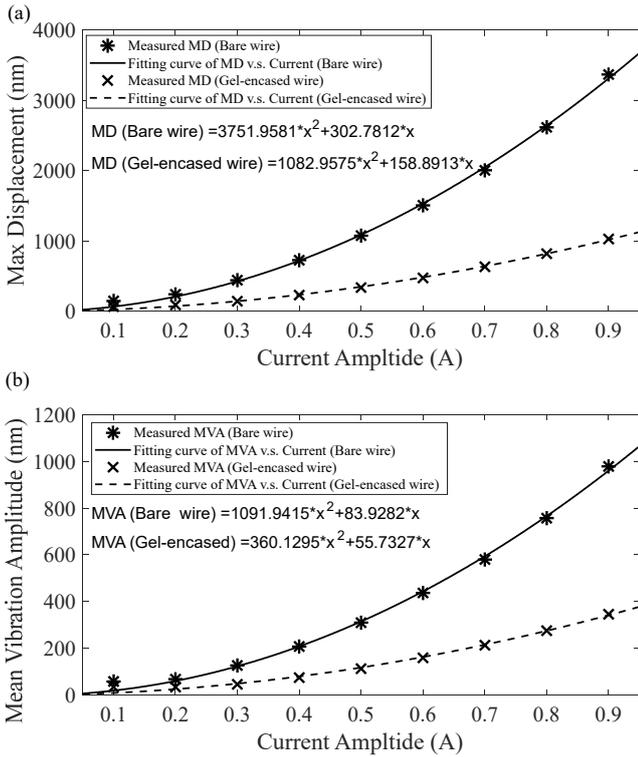
Fig. 6. Measured displacement and corresponding fitting curve of bare and gel-encased wire under different pulse current amplitudes, (a) max displacement; (b) mean vibration amplitude.

from the other curves in both bare and gel-encased wire. Fig. 6 shows the measured values and corresponding fitting curve of MD and mean vibration amplitude (MVA) of bare/gel-encased wire. The MD and MVA values of bare wire are also always larger than the MD and MVA of gel-encased wire in each current amplitude. In addition, it was found in all cases that the vertical displacement of bare wire is always larger than the that of gel-encased wire.

In order to analyse wire deformation characteristics under different pulse frequencies, we carried out measurement at two frequencies whilst keeping the pulse current amplitude and duty cycle constant at 500 mA and 50% respectively. Fig. 7 and Table I illustrate the vertical displacement and displacement change percentage measured at 5 Hz and 10 Hz, respectively. As shown in Fig. 7, the MD is similar between deformation excited by 5 Hz and 10 Hz pulse in both bare and gel-encased wire. The reason is that the heating accumulation and corresponding total deformation within the same period is relevant to the current amplitude and duty cycle. Moreover, since higher frequency leads to shorter heating and cooling period in each pulse cycle, the value of VA in 10 Hz is around half of the VA in 5 Hz. Thus, higher current pulse frequency leads to smaller deformation of the bonding wire, which might reduce the effect of repetitive ETM deformation on the lifetime. The previous research [41] also agreed that the lifetime of PEMs increases for shorter load pulse duration or higher current pulse frequency. They proved this mechanism by setting the PEMs to work with two different output current frequencies. The frequency of output current is corresponding to the frequency of the repetitive
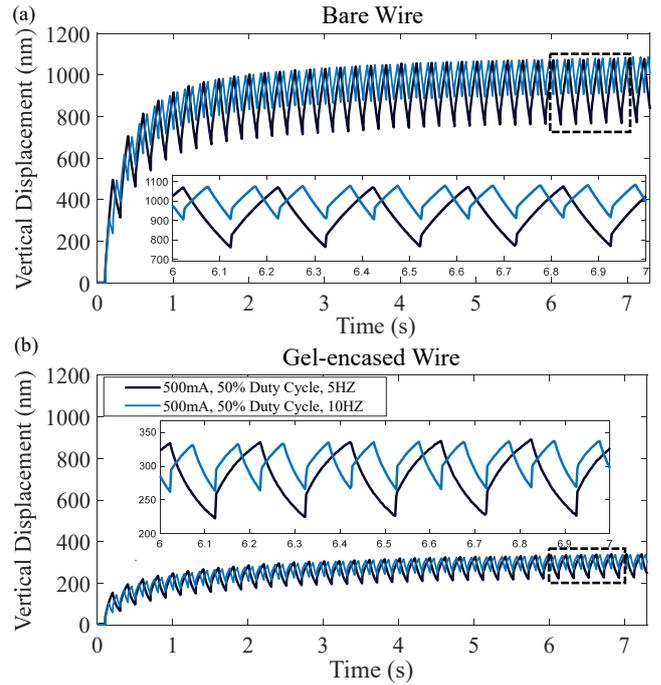
Fig. 7. Vertical displacement of the wire under 5 Hz and 10 Hz frequencies of pulse current: (a) bare wire; (b) encased with silicone gel.

TABLE I
MAX DISPLACEMENT AND MEAN VIBRATION AMPLITUDE IN DIFFERENT PULSE CURRENT FREQUENCIES

Frequency (Hz)	5	10
MD without gel (nm)	1077	1086
MD under gel (nm)	339	339
Change of MD (%)	68.6	68.8
MVA without gel (nm)	310	172
MVA under gel (nm)	113	70
Change of MVA (%)	63.5	59.3

ETM stress in the PEM. The PEMs with higher output current frequency have longer lifetime than the PEMs with lower output current frequency.

Fig. 8 shows the vertical displacement of wire under 500 mA, 5 Hz pulse current with three different duty cycles (20%, 50% and 80%). The three displacement curves are overlapped at the beginning due to the same current amplitude and pulse frequency. The MD of displacements within the measurement period increases with the value of the duty cycle because the higher duty cycle generates more heat in the wire. The MVA of 50% duty cycle pulse current is higher than the MVA of 20% and 80% duty cycle. Regarding the fixed current amplitude and pulse frequency, the 20% duty cycle pulse accumulates less heat in each pulse than 50% duty cycle pulse. Meanwhile, less heat accumulation results in a smaller temperature difference between the environment and the wire, which indicates a lower heat dissipation rate. Thus, the MVA of 20% duty cycle pulse is smaller than the MVA of 50% duty cycle pulse. For the VA

(a) Bare Wire

(b) Gel-encased Wire
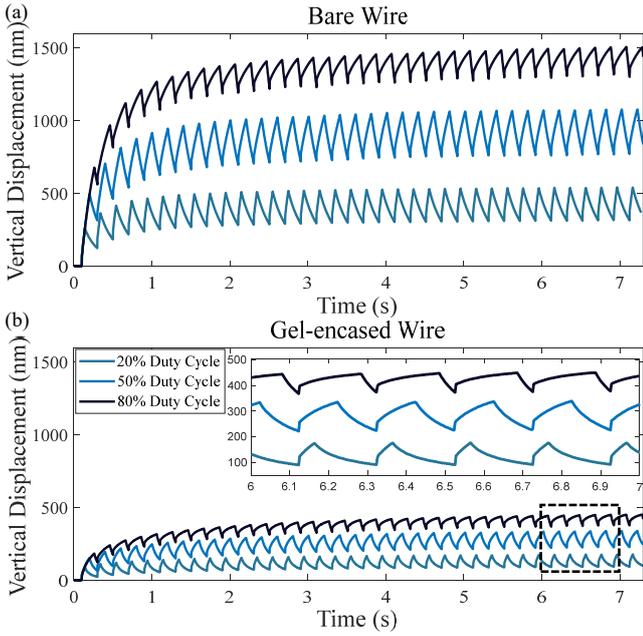
Fig. 8. Vertical displacement of the wire under different duty cycle values (a) bare wire; (b) encased with silicone gel.

TABLE II
MAX DISPLACEMENT AND MEAN VIBRATION AMPLITUDE
IN DIFFERENT DUTY CYCLE VALUES

Duty Cycle (%)	20	50	80
MD without gel (nm)	542	1077	1509
MD under gel (nm)	178	339	452
Change of MD (%)	67.3	68.6	70.1
MVA without gel (nm)	226	310	201
MVA under gel (nm)	84	113	78
Change of MVA (%)	62.8	63.5	61.2

excited by 80% duty cycle pulse, the period of the cooling process is shorter than the 50% duty cycle pulse; the heat dissipation rate increased with the heat accumulation, which slows down the upward deformation rate of the wire. Hence, the MVA of 50% duty cycle pulse is larger than the MVA of 80% duty cycle pulse. Consequently, VA relates to the equilibrium state between heat accumulation and heat dissipation of each pulse.

As shown in Fig. 5-8, the ETM deformation of the gel-encased wire is three times smaller than that of the bare wire. This agrees with previous work where the mold/encapsulant around the wire has been demonstrated to reduce the temperature swings on the wire [42, 43]. Since the thermal conductivity and corresponding heat transfer coefficient of mold/encapsulant are larger than air, the current-induced temperature on the wire is reduced. As a result, the thermal expansion of the wire is reduced as well. Therefore, the encapsulant such as silicone gel can conduct/absorb the generated heat on the wire, which reduces the temperature-induced deformation of the wire. Meanwhile, the damping ability of silicone gel also affects the deformation of the wire. Thus, our LF-OCT measurement results

provide direct experimental evidence for the deformation reduction ability of silicone gel, and different pulse profiles result in different thermal/stress accumulation on the bonding wire. Thus, the load pulse profile can affect the lifetime of the PEM, as has been shown in previous studies [41, 44, 45].

C. Theoretical and Measured Vertical Displacement Comparison

To understand the underlying mechanisms of the observed wire deformation, we define the displacement induced by the first pulse as initial displacement and calculate the initial displacement using FEM simulations (shown in Fig. 9). A diagram of wire deformation excited by a pulse current is depicted in Fig. 9(a). The vertical displacement is composited by the length and diameter changes of the wire via thermal expansion. For comparison against the measured deformation data, a FEM model was built in COMSOL. Fig. 9(b) shows the gel-encased wire model. The two terminals of copper wire are fixed on the glass slide. The shape of the wire loop was determined by the sample, which was modelled as a three-order of Bessel curve in the model. The projected length of wire loop L_p was set to 12 mm, and the loop height H was set to 1.1 mm. The thickness of the gel covering H_g is set to 1.4 mm. For the bare wire model, the gel part was changed to air. The thermal distribution and temperature swings were simulated at first. Fig. 9(c) shows the simulated temperature distribution of gel-encased wire at the time of 2 s, where the wire was excited by 900 mA, 5 Hz and 50% duty cycle pulse current. Subsequently, the resultant wire ETM deformation was calculated accordingly, which is shown in Fig. 9(d). According to the measurement and simulation results, the measured vertical displacement is dominated by the length changes of the wire. Table III lists the values of the critical parameters used in the simulation. Where c is the specific heat, D is the mass density, σ_{cu} is the conductivity of copper, T_{amb} is the ambient temperature, h is convective heat transfer coefficient, and K is the thermal conductivity.

The simulated initial displacement of bare and gel-encased wire excited by different current amplitudes are shown as the black solid and dash lines in Fig. 9(e). The simulation results are compared with the measured initial displacement of bare and gel-encased wire (under the same 5 Hz and 50% duty cycle pulses). It was found that the vertical displacements measured by the LF-OCT system are close to that calculated from the FEM simulation. The difference between simulated and measured values could be resulted from the difference between parameter settings of the real conditions and the simulated conditions. For example, the mechanics properties of the gel are affected by curing conditions and temperature during the experiments. In addition, the current pulse applied in the simulation is a perfect square wave whilst in practice transient peak current may exist.

Additionally, the shape of measured displacement curve is closed to the simulated temperature changes on a bonding wire by numerical calculation in [43], which also validates that the measured displacement is caused by the ETM stress but not random vibration errors from the experiment environment. Our FEM simulation results also revealed that the shape of the
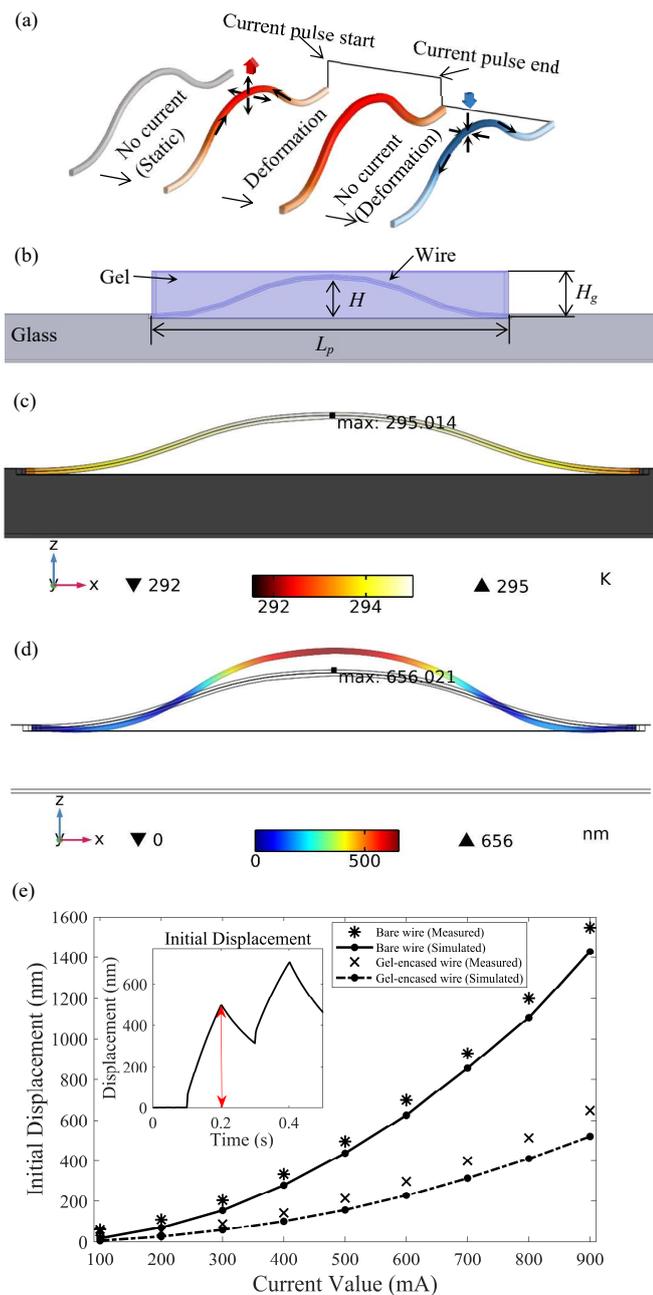
Fig. 9. (a) Deformation process of wire; (b) FEM model build in COMSOL; (c) Temperature distribution; (d) deformation of the wire; (e) Measured initial displacement and simulated initial displacement at different current amplitudes of 5 Hz 50% Duty Cycle pulse of bare wire and gel-encased wire.

measured vertical displacement (the bonding wire deformation) is similar to that of the calculated temperature swings on the boding wire. This further suggests that the measured displacement, which is periodic, is indeed caused by electrical-thermal expansion of the bonding wire, rather than random vibration errors.

As demonstrated here, the high-resolution and high-speed image acquisition of the LF-OCT system provides unique quantitative experimental data that can be used to validate future numerical simulations of the ETM deformation dynamics of both bare and gel-encased bonding wires. Note that although the sample used in this paper is a copper wire of a diameter of 120 μm as a demonstration of proof-of-principle, the proposed method will be applicable to the heavy-duty bonding wires such as aluminium wires of diameter of 300 μm or 500 μm commonly employed in PEMs. The proposed method directly detects the deformation/displacement of the bonding wires with a detection range of up to 2 mm and a detection sensitivity of 0.1 nm. With such a large detection range the method will be applicable to the study of the deformation excited by large current, for example, an Al wire excited by 10 to 20 A current.

The bonding wire deformation or ETM stress-induced component deformation can be characterised and analysed without removing the silicone gel. Since the measured ETM deformation correlates to the temperature swings on the wire, according to Coffin-Mason Law and lifetime prediction model in [46], the measured ETM deformation (strain on the wire) correlates to the number of cycles-to-failure of PEMs. As a result, the LF-OCT not only can assess the silicone gel deformation reduction ability for bonding wire, but also has the potential to investigate bonding wires reliability by measuring and analysing the ETM deformation profile.

IV. CONCLUSION

We reported in this paper the first experimental demonstration that the LF-OCT can be used to quantitatively study the ETM deformation of both bare and silicone gel-encased wires. Since silicone gel is widely used to protect the bonding wire, it is important to understand the influence of silicone gel on bonding wire deformation. By utilising the Fourier phase self-referencing method, the LF-OCT can measure the deformation of the bare and gel-encased wire caused by the ETM stress down to nanometre scale. The experimental results indicate that the gel-encased wire has approximately three times smaller ETM deformation than the bare wire, under the same pulse current settings. Therefore, this work provides a direct experimental evidence of that silicone gel can reduce bonding wire deformation by reducing the local temperature on the bonding wire. The influence of different pulse current frequencies, amplitudes, and duty cycle values on the ETM deformation of the wire have also been studied. The MD and VA, which indicate the maximum

and repetitive deformation on the wire, are found to correlate with the duty cycle, frequency, and current amplitude. In conclusion, this study proposes a non-destructive method to facilitate bonding wire reliability analysis and silicone gel characterisation on deformation reduction property.

The proposed method could be used for the investigation of bonding wire reliability, faults detections of bonding wires, and assessment of silicone gel deformation reduction ability. These applications could help the development and reliability assessment of future power electronics devices. In particular, since the next generation of power electronics employ the wide bandgap semiconductors that work at high temperature, the proposed LF-OCT method could be used to investigate the deformation reduction ability of high-temperature silicone gel thus providing vital information for the design optimisation of the next generation PEM. The deformation comparisons of the wire encased by different types of silicone gel will also be carried out.

REFERENCES

[1] J. G. Kassakian and T. M. Jahns, "Evolving and emerging applications of power electronics in systems," *IEEE Journal of Emerging and Selected Topics in Power Electronics,* vol. 1, no. 2, pp. 47-58, 2013.

[2] H. Oh, B. Han, P. McCluskey, C. Han, and B. D. Youn, "Physics-of-failure, condition monitoring, and prognostics of insulated gate bipolar transistor modules: A review," *IEEE Transactions on power electronics,* vol. 30, no. 5, pp. 2413-2426, 2014.

[3] H. Lu, C. Bailey, and C. Yin, "Design for reliability of power electronics modules," *Microelectronics reliability,* vol. 49, no. 9-11, pp. 1250-1255, 2009.

[4] Y. Avenas, L. Dupont, N. Baker, H. Zara, and F. Barruel, "Condition monitoring: A decade of proposed techniques," *IEEE Industrial Electronics Magazine,* vol. 9, no. 4, pp. 22-36, 2015.

[5] S. Yang, D. Xiang, A. Bryant, P. Mawby, L. Ran, and P. Tavner, "Condition monitoring for device reliability in power electronic converters: A review," *IEEE Transactions on Power Electronics,* vol. 25, no. 11, pp. 2734-2752, 2010.

[6] K. Sasaki and N. Ohno, "Fatigue life evaluation of aluminum bonding wire in silicone gel under random vibration testing," *Microelectronics Reliability,* vol. 53, no. 9-11, pp. 1766-1770, 2013.

[7] B. Ji, V. Pickert, W. Cao, and B. Zahawi, "In situ diagnostics and prognostics of wire bonding faults in IGBT modules for electric vehicle drives," *IEEE Transactions on Power Electronics,* vol. 28, no. 12, pp. 5568-5577, 2013.

[8] M. Ciappa, "Selected failure mechanisms of modern power modules," *Microelectronics reliability,* vol. 42, no. 4-5, pp. 653-667, 2002.

[9] S. Ramminger, P. Türkes, and G. Wachutka, "Crack mechanism in wire bonding joints," *Microelectronics Reliability,* vol. 38, no. 6-8, pp. 1301-1305, 1998.

[10] L. Yang, P. A. Agyakwa, and C. M. Johnson, "Physics-of-failure lifetime prediction models for wire bond interconnects in power electronic modules," *IEEE Transactions on Device and Materials Reliability,* vol. 13, no. 1, pp. 9-17, 2012.

[11] Y. Huang, Y. Jia, Y. Luo, F. Xiao, and B. Liu, "Lifting-off of Al bonding wires in IGBT modules under power cycling: failure mechanism and lifetime model," *IEEE Journal of Emerging and Selected Topics in Power Electronics,* 2019.

[12] U.-M. Choi, F. Blaabjerg, and S. Jørgensen, "Power cycling test methods for reliability assessment of power device modules in respect to temperature stress," *IEEE Transactions on Power Electronics,* vol. 33, no. 3, pp. 2531-2551, 2017.

[13] J. Onuki, M. Koizumi, and M. Suwa, "Reliability of thick Al wire bonds in IGBT modules for traction motor drives," *IEEE Transactions on Advanced Packaging,* vol. 23, no. 1, pp. 108-112, 2000.

[14] V. Smet *et al.*, "Ageing and failure modes of IGBT modules in high-temperature power cycling," *IEEE transactions on industrial electronics,* vol. 58, no. 10, pp. 4931-4941, 2011.

[15] E. Arjmand, P. A. Agyakwa, M. R. Corfield, J. Li, B. Mouawad, and C. M. Johnson, "A thermal cycling reliability study of ultrasonically bonded copper wires," *Microelectronics Reliability,* vol. 59, pp. 126-133, 2016.

[16] K. Li, G. Y. Tian, L. Cheng, A. Yin, W. Cao, and S. Crichton, "State detection of bond wires in IGBT modules using eddy current pulsed thermography," *IEEE Transactions on Power Electronics,* vol. 29, no. 9, pp. 5000-5009, 2013.

[17] N. Baker, L. Dupont, S. Munk-Nielsen, F. Iannuzzo, and M. Liserre, "IR camera validation of IGBT junction temperature measurement via peak gate current," *IEEE Transactions on Power Electronics,* vol. 32, no. 4, pp. 3099-3111, 2016.

[18] B. Czerny, M. Lederer, B. Nagl, A. Trnka, G. Khatibi, and M. Thoben, "Thermo-mechanical analysis of bonding wires in IGBT modules under operating conditions," *Microelectronics Reliability,* vol. 52, no. 9-10, pp. 2353-2357, 2012.

[19] K. B. Pedersen and K. Pedersen, "Dynamic modeling method of electro-thermo-mechanical degradation in IGBT modules," *IEEE Transactions on Power Electronics,* vol. 31, no. 2, pp. 975-986, 2015.

[20] Y. Jia, F. Xiao, Y. Duan, Y. Luo, B. Liu, and Y. Huang, "PSpice-COMSOL Based 3D Electro-Thermal-Mechanical Modeling of IGBT Power Module," *IEEE Journal of Emerging and Selected Topics in Power Electronics,* 2019.

[21] N. Dornic *et al.*, "Stress-Based Model for Lifetime Estimation of Bond Wire Contacts Using Power Cycling Tests and Finite-Element Modeling," *IEEE Journal of Emerging and Selected Topics in Power Electronics,* vol. 7, no. 3, pp. 1659-1667, 2019.

[22] Y. Yao, G.-Q. Lu, D. Boroyevich, and K. D. Ngo, "Survey of high-temperature polymeric encapsulants for power electronics packaging," *IEEE Transactions on Components, Packaging and Manufacturing Technology,* vol. 5, no. 2, pp. 168-181, 2015.

[23] Z. Liu, J. Li, and X. Liu, "Novel functionalized BN nanosheets/epoxy composites with advanced thermal conductivity and mechanical properties," *ACS applied materials interfaces,* vol. 12, no. 5, pp. 6503-6515, 2020.

[24] H. Lu, W.-S. Loh, C. Bailey, and C. M. Johnson, "Computer simulation of aluminium wirebonds with globtop in power electronics modules," in *2008 3rd International Microsystems, Packaging, Assembly & Circuits Technology Conference*, 2008, pp. 348-351: IEEE.

[25] A. F. Fercher, W. Drexler, C. K. Hitzenberger, and T. Lasser, "Optical coherence tomography-principles and applications," *Reports on progress in physics,* vol. 66, no. 2, p. 239, 2003.

[26] J. Czajkowski, T. Prykäri, E. Alarousu, J. Palosaari, and R. Myllylä, "Optical coherence tomography as a method of quality inspection for printed electronics products," *Optical review,* vol. 17, no. 3, pp. 257-262, 2010.

[27] J. Czajkowski *et al.*, "Ultra-high resolution optical coherence tomography for encapsulation quality inspection," *Applied Physics B,* vol. 105, no. 3, pp. 649-657, 2011.

[28] Y.-J. Lee, C.-Y. Chou, C.-Y. Huang, Y.-C. Yao, Y.-K. Haung, and M.-T. Tsai, "Determination on the Coefficient of Thermal Expansion in High-Power InGaN-based Light-emitting Diodes by Optical Coherence Tomography," *Scientific reports,* vol. 7, no. 1, pp. 1-9, 2017.

[29] Z. Yaqoob *et al.*, "Improved phase sensitivity in spectral domain phase microscopy using line-field illumination and self phase-referencing," *Optics express,* vol. 17, no. 13, pp. 10681-10687, 2009.

[30] A. F. Zuluaga and R. Richards-Kortum, "Spatially resolved spectral interferometry for determination of subsurface structure," *Optics letters,* vol. 24, no. 8, pp. 519-521, 1999.

[31] S. Lawman *et al.*, "High resolution corneal and single pulse imaging with line field spectral domain optical coherence tomography," *Optics express,* vol. 24, no. 11, pp. 12395-12405, 2016.

[32] S. Lawman, B. M. Williams, J. Zhang, Y.-C. Shen, and Y. Zheng, "Scan-less line field optical coherence tomography, with automatic image segmentation, as a measurement tool for automotive coatings," *Applied Sciences,* vol. 7, no. 4, p. 351, 2017.

[33] L. Han, Z. Hosseiaee, B. Tan, and K. Bizheva, "High resolution line-field SD-OCT with 2.5 kHz frame rate for cellular resolution imaging of biological tissue," in *Optical Coherence Tomography and Coherence Domain Optical Methods in Biomedicine XXIII*, 2019, vol. 10867, p. 108672X: International Society for Optics and Photonics.

[34] Y. Celnikier, L. Benabou, L. Dupont, and G. Coquery, "Investigation of the heel crack mechanism in Al connections for power electronics modules," *Microelectronics reliability,* vol. 51, no. 5, pp. 965-974, 2011.

[35] S. Lawman and H. Liang, "High precision dynamic multi-interface profilometry with optical coherence tomography," *Applied optics,* vol. 50, no. 32, pp. 6039-6048, 2011.

[36] M. Hanson and A. Wypych, "Databook of Curatives & Crosslinkers," ChemTec Publishing, 2019, p. 174.

[37] M. A. Choma, A. K. Ellerbee, C. Yang, T. L. Creazzo, and J. A. Izatt, "Spectral-domain phase microscopy," *Optics letters,* vol. 30, no. 10, pp. 1162-1164, 2005.

[38] C. Joo, T. Akkin, B. Cense, B. H. Park, and J. F. De Boer, "Spectral-domain optical coherence phase microscopy for quantitative phase-contrast imaging," *Optics letters,* vol. 30, no. 16, pp. 2131-2133, 2005.

[39] S. Uttam and Y. Liu, "Fourier phase in Fourier-domain optical coherence tomography," *JOSA A,* vol. 32, no. 12, pp. 2286-2306, 2015.

[40] S. Lawman *et al.*, "Deformation velocity imaging using optical coherence tomography and its applications to the cornea," *Biomedical optics express,* vol. 8, no. 12, pp. 5579-5593, 2017.

[41] U. Scheuermann and R. Schmidt, "Impact of load pulse duration on power cycling lifetime of Al wire bonds," *Microelectronics Reliability,* vol. 53, no. 9-11, pp. 1687-1691, 2013.

[42] W. Childres and G. Peterson, "Quantification of thermal contact conductance in electronic packages," *IEEE transactions on components, hybrids, and manufacturing technology,* vol. 12, no. 4, pp. 717-723, 1989.

[43] C. C. Jung, C. Silber, and J. Scheible, "Heat generation in bond wires," *IEEE Transactions on Components, Packaging and Manufacturing Technology,* vol. 5, no. 10, pp. 1465-1476, 2015.

[44] U.-M. Choi, S. Jørgensen, and F. Blaabjerg, "Advanced accelerated power cycling test for reliability investigation of power device modules," *IEEE Transactions on Power Electronics,* vol. 31, no. 12, pp. 8371-8386, 2016.

[45] R. Bayerer, T. Herrmann, T. Licht, J. Lutz, and M. Feller, "Model for power cycling lifetime of IGBT modules-various factors influencing lifetime," in *5th International Conference on Integrated Power Electronics Systems*, 2008, pp. 1-6: VDE.

[46] C. Busca *et al.*, "An overview of the reliability prediction related aspects of high power IGBTs in wind power applications," *Microelectronics reliability,* vol. 51, no. 9-11, pp. 1903-1907, 2011.

Zhiyi Zhao was born in Tianjin, China. He received the B.Eng. Degree in Electrical Engineering from Xi'an Jiaotong-Liverpool University (XJTLU), Suzhou, China, in 2017, and B.Eng. Degree (1st Hons.) in Electrical and Electronics Engineering from the University of Liverpool (UoL), Liverpool, U.K., in 2017. He is currently pursuing the Ph.D. degree in Electrical Engineering and Electronics with the University of Liverpool.

From October 2019 to March 2020, he worked as a Research Assistant at the University of Liverpool, where he developed the Line-field Optical Coherence Tomography (LF-OCT) system for non-destructive testing. His research interests include OCT system development, non-destructive testing, and power electronics devices reliability.

Zijian Zhang was born in Beijing, China. He received the B.Eng. degree in detection guidance and control technology from the North University of China, Shanxi, China, in 2009. He received the M.Sc. and Ph.D. degrees in electrical engineering and electronics from the University of Liverpool, Liverpool, U.K., in 2011 and 2019, respectively.

In 2012, for three years, he worked as an algorithm designer in the China Academy of Space Technology, Beijing, China. He is currently a Research Associate in the Department of Electrical Engineering and Electronics at the University of Liverpool, Liverpool, U.K. His research interests have revolved around developing high-performance and cost-effective Optical Coherence Tomography (OCT) variants for ophthalmic applications, and exploring innovative applications with OCT techniques for other industrial areas.

Samuel James Lawman received a BSc (Hons) degree in Physics from the University of Hull in 2006, an optics orientated course. He was awarded his PhD from Nottingham Trent University in 2011, a project in collaboration with the National Gallery, London, using optical coherence tomography, amongst other techniques, to study how the material properties of varnishes effect the appearance of paintings. He then worked for a period for a SME rubber compounder managing and developing ISO 9001 systems. He is currently a PDRA at the University of Liverpool on consecutive NIHR funded projects with the aim of bringing a concept optical coherence tomography design to clinical trial and onto the market. He is a named author on over 10 journal papers and 2 patent applications, with over 150 recorded citations on Google Scholar.

Zhihao Yin received B.Eng. degree in electrical engineering and automation from the Yangtze University, Jingzhou, China, in 2019. He is currently a first-year postgraduate student at the University of Chinese Academy of Sciences. His main research interests are micro-nano detection instruments and failure characterization of power electronic modules.

Yihua Hu received the B.S. degree in electrical engineering in 2003, and the Ph.D. degree in power electronics and drives in 2011, both at China University of Mining and Technology. Between 2011 and 2013, he was with the College of Electrical Engineering, Zhejiang University as a Postdoctoral Fellow. Between 2013 and 2015, he worked as a Research Associate at the power electronics and motor drive group, the University of Strathclyde. Between 2016 and 2019, he was a Lecturer at the Department of Electrical Engineering and Electronics, University of Liverpool (UoL). Currently, he is a Reader at Electronics Engineering Department at The University of York (UoY). He has published over 100 papers in IEEE Transactions journals. His research interests include renewable generation, power electronics converters & control, electric vehicle, more electric ship/aircraft, smart energy system and non-destructive test technology. He is the associate editor of IEEE Transactions on Industrial Electronics, IET Renewable Power Generation, IET Intelligent Transport Systems and Power Electronics and Drives. He is a fellow of Institution of Engineering and Technology (FIET). He was awarded Royal Society Industry Fellowship.

Ju Xu is currently a senior staff researcher in Institute of Electrical Engineering (IEE), Chinese Academy of Sciences (CAS) and a professor in the department of Engineering, University of Chinese Academy of Sciences (UCAS). She is a recipient of the Newton Advanced Fellowship funded by the royal society, UK. She obtained her Ph.D. degree in Department of Chemistry from University of College Cork, Ireland in 2008, her M.Sc. degrees from Institute of Process Engineering, Chinese Academy of Sciences in 2001 and her B.E. in Department of Chemical Engineering from Nanchang University in 1997. Before joining in IEE in 2013, she was a research fellow (2007-2013) in Microelectronic System Centre, Tyndall National Institute, Ireland and an Ircset-Marie Curie Research Fellow (2010-2012) in 3D Systems Packaging Research Center, George W. Woodruff School of Mechanical Engineering, Georgia Institute of Technology, USA. Dr. Ju Xu specializes in the

area of materials and technologies on power electronic packaging. Her current research interests mainly focuses on materials and technologies on high temperature power electronics packaging. Dr. Xu has an h-index of 12 according to ISI report. And she is an author of over 40 peer reviewed journal publications, 4 filed patents and 10 other conference articles. Those publications have attracted more than 200 citations.

Yao-chun Shen received his PhD, MSc and BSc degrees in electronics from Nanjing University, China. After that he held various positions at Southeast University (China), Heidelberg University (Germany), Heriot-Watt University (UK), Cambridge University (UK) and TeraView Ltd (UK). Since 2006, he has been with University of Liverpool (UK) where he is currently a Chair Professor of the Department of Electrical Engineering and Electronics. Prof Shen has been awarded 7 patents and published 5 book chapters and over 200 conference & journal publications with an h-index of 45. His current research interests include the development of innovative terahertz and optical imaging technologies with a focus on the exploitation of their applications in industry and science. Prof. Shen is Fellow of IET and he served as Editor for Sensor Networks and Data Communications, and Guest Editor for Applied Sciences and for IET Microwaves, Antennas & Propagation.